Lawrence Berkeley Laboratory
UNIVERSITY OF CALIFORNIA

Physics, Computer Science & Mathematics Division
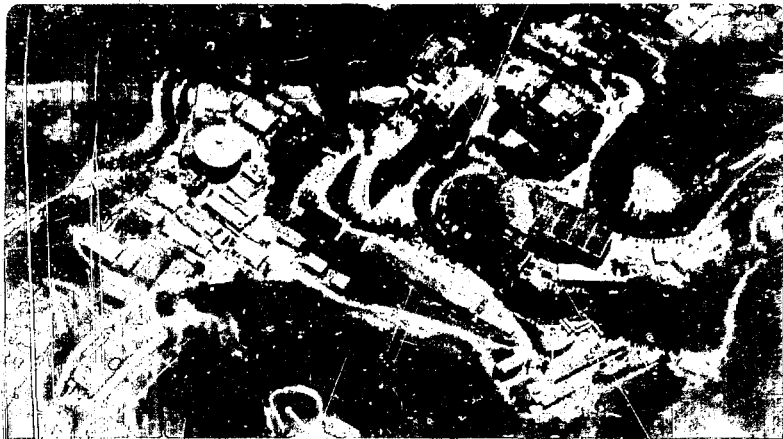
MASTER

THE IMAGING PERFORMANCE OF A MULTIWIRE PROPORTIONAL-
CHAMBER POSITRON CAMERA

Victor Perez-Mendez, Alberto Del Guerra,
Walter R. Nelson, and Kwok C. Tam

August 1982

THE IMAGING PERFORMANCE OF A MULTIWIRE PROPORTIONAL-CHAMBER POSITRON CAMERA[(+)]

Victor Perez-Mendez[(1,2)], Alberto Del Guerra[(1,*)], Walter R. Nelson[(3)], and Kwok C. Tam[(4)]

(1) Lawrence Berkeley Laboratory, Berkeley, CA. 94720; (2) Department of Radiology, UCSF, San Francisco, CA. 94143; (3) Stanford Linear Accelerator Center, Stanford, CA. 94305; (4) General Electric Co., Schenectady, NY 12345.

ABSTRACT

A new design — fully three dimensional - Positron Camera is presented, made of six MultiWire Proportional Chamber modules arranged to form the lateral surface of a hexagonal prism. A true coincidence rate of 56000 c/s is expected with an equal accidental rate for a 400 µCi activity uniformly distributed in a $\sim 3\ell$ water phantom. A detailed Monte Carlo program has been used to investigate the dependence of the spatial resolution on the geometrical and physical parameters. A spacial resolution of 4.8 mm FWHM has been obtained for a ^{18}F point-like source in a 10 cm radius water phantom. The main properties of the limited angle reconstruction algorithms are described in relation to the proposed detector geometry.

1. Introduction

The technique of tomographical imaging with x-rays[(1,2)] has now become an essential tool of any major medical center. Although tomographical imaging originated in practice in early nuclear medicine laboratories[(3,4)], its application lagged behind, due to technological difficulties. In fact, only after CT-scanners came into operation has research in this field become appreciable and have the first positron tomography cameras been developed in USA[(5-9)] and European[(10)] laboratories. A number of positron tomographs have been constructed and are now used for medical research. Most of these are single ring scintillator detectors, using either sodium iodide[(11,12)] or bismuth germanate crystals[(13,14)]. More recently cesium fluoride crystals have been used[(15-17)] because of their fast time response. It is usually necessary to measure more than one slice of the object; this can be done either by a series of parallel strip images taken sequentially, or by making large area detectors or multi-ring detectors (which are much more expensive to build than single section tomographs).

In this paper we propose a new design for a large area positron camera and discuss its expected imaging performance, which has been evaluated both by experimental measurements and by Monte Carlo simulation. The proposed large area concentric detector is conceived to measure a sensitive volume of ~ 3 liters. The detector is based on a MWPC with lead glass drift space converters.

In the next section a description of the camera is given and a brief summary of the experimental results is reported. Section 3 deals with the Monte Carlo simulation of the detector and the results are presented in section 4. Limited angle reconstruction algorithms will be used to produce tomographical imaging of the real data. The main features of such algorithms, as applied to this detector, are described in section 5. Finally, some concluding remarks are given in the last section.

2. The MWPC Positron Camera

A schematic drawing of the proposed camera is shown in Fig. 1. Six modules (each 50×50 cm^2) are arranged to form the lateral surface of a hexagonal prism. Following the annihilation of the positron within the target, two γ-rays are produced, each with an energy of 511 keV and opposite to the other within a few mrad. A good event results when both gammas are detected "in coincidence" in opposite modules. Each module consists of a standard MWPC (45×45 cm^2 active area), with a 2 cm thick lead glass tube converter on each side (Fig. 1).

2.1 Principle of Operation of a Dense Drift Space MWPC

The detection of 511 keV γ-rays with a MWPC requires the use of a high density, high Z converter with large surface to volume ratio. We have developed a converter made of glass capillaries (0.9 mm inner diameter, 0.096 mm wall thickness) of high lead content (80% PbO by weight, glass density of 6.2 g/cm^3), fused to form honeycomb matrices[(18)]. The lead glass matrices are treated in a H$_2$ reduction process to form a uniform resistive layer on the inner walls of each tube. The Compton- or photo-electron produced by the photon interacting within the converter has a finite range dependent upon its energy. If it reaches the gas region within the tube, a number of primary ionization electrons are produced. A voltage difference applied between the ends of the tubes then drifts these primary electrons along the electric field lines within the tube towards the cathode planes and into the avalanche region of the chamber.
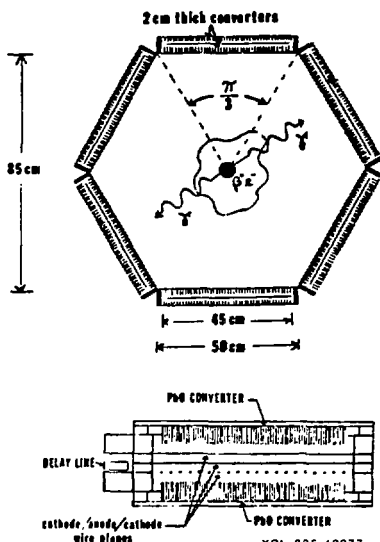
Fig. 1 - Proposed Positron Camera made of six modules arranged to form a hexagonal prism: plan view of the camera (TOP), cross view of a single module (BOTTOM).

2.2 Experimental Results

We have built two 50 × 50 cm² modules and some experimental measurements have been taken. For convenience we have extensively tested a smaller module (15 × 15 cm² active area) equipped with one 1 cm thick converter. The chamber itself is a standard gas filled MWPC with the two cathode planes at 90° to each other in order to have both x and y localization. Position readout is achieved by means of fast delay lines (8 ns/cm) coupled to the cathode planes[19]. The experimental details have already been reported[20-22]. Table 1 briefly summarizes the results obtained with a standard argon-methane (70-30) gas mixture at 2 atm for 511 keV γ-rays incident perpendicular onto the module plane. In order to extrapolate these results to converters of different thickness we assume that the efficiency is proportional to the γ interaction probability, whereas the time resolution is determined by the transit time of the electrons within the converter tubes. For the same electron drift velocity in the gas (i.e. the same value of the reduced electric field), the transit time is then proportional to converter thickness. The expected performance of the Positron Camera module is also presented in Table 1. The gas pressure will be kept at 2 atm in order to take advantage of the self quenching streamer regime[23,24].

2.3 Count Rates of the Tomograph

It is well known that given a pure positron emitting source and two opposite γ-ray detectors, both the single rate and the true coincidence rate are proportional to the source strength. If the solid angle fraction (f_Ω) subtended at the source is the same for both detectors and if the efficiency (ϵ) for 511 keV γ-rays is the same and constant within the solid angle, one gets

$$N_1 = N_2 = (2S)f_\Omega\epsilon \qquad (1a)$$
$$T = S \quad (2f_\Omega)\epsilon^2 \qquad (1b)$$
$$A = N_1 \quad N_2 \quad (2\tau) \qquad (1c)$$

where N_1 and N_2 are the single rate of the detectors, S is the source strength, T and A on the true and accidental coincidence rates respectively, and τ is the resolving time of coincidence.

It is conventional to express the figure-of-merit parameter of a positron camera by giving the ratio ϵ^2/τ. One obtains the following relation, which applies to a module pair:

$$T^2/A = \epsilon^2/2\tau \qquad (2)$$

For a given set of detector parameters T/A is inversely proportional to the source strength:

$$\frac{T}{A} = \frac{1}{S \quad 4 \quad f_\Omega \ \tau} \qquad (3)$$

For a signal to noise ratio

$$\frac{T}{A} = 1 \qquad (4)$$

Table 1
Specification and Performance of the Test Module and of the Positron Camera Module

	Test Module	Positron Camera Module
MWPC active area (cm²)	15 × 15	45 × 45
Converter thickness (cm)	1	2 + 2
Gas pressure (atm)	2.0	2.0
Efficiency (%)	4.5	15.0
Time resolution (ns)	130	200[(**)]
Spatial resolution FWHM		
-along the coordinate parallel		
to the anode wires (mm)	1.3	
		2.0
-along the other coordinate (mm)	2.0	

(**) Using a 20% faster gas mixture according to ref. 20.

the value of the source strength is given by

$$S|_{T/A=1} = \frac{1}{4\ f_\Omega\ \tau} \qquad (5)$$

For our detector, one gets a value of
~400 μCi, which represents the maximum source
strength we can use for a signal to noise ratio
≥ 1. Using condition (4), equation (2) becomes

$$\tau|_{T/A=1} \sim \epsilon^2/2\tau \qquad (6)$$

which gives the maximum true coincidence rate
per module pair compatible with condition (4).
The expected count rates in air and with a 10 cm
radius water phantom are listed in Table 2. The
effect of the absorbing medium is equivalent to
decreasing the efficiency of each detector (as
determined by using the Monte Carlo program
described in section 3). Hence, the net result
of the absorption and scattering in the phantom
is to decrease the statistics, while keeping the
same signal to noise ratio.

3. Monte Carlo Technique and Problem Model

3.1 The EGS Code: General Considerations

To study the spatial resolution properties
of the tomograph, a general electromagnetic
radiation transport code called EGS
(Electron-Gamma-Shower)[25] was implemented
for the problem at hand. EGS is currently being
used to solve a variety of problems in
accelerator, high-energy, and medical
physics[26]. In particular, EGS is capable of
treating electrons, positrons and photons with
kinetic energy as low as 10 keV (electrons and
positrons) and 1 keV (photons). The transport
can take place in any of one hundred different
elements or in any mixture or compound of these
elements. It is left to the user to construct
his own geometry and to score a particular
answer.

For the problem at hand, the hexagonal
3-dimensional geometry of the positron camera
was simulated. In what follows, we will limit
ourselves to the results obtained for a
point-like source at the center of a 10 cm
radius water phantom. The simulation may be
subdivided into three main modes of operation:
- generation, transport, and annihilation of
  the positron,
- transport (including interaction) of the
  annihilation quanta within the phantom
  and the detector,

- scoring of coincidence events and
  production of spatial resolution
  histograms.

As many as 200 positrons per second are
generated and "followed" up to the scoring point
on the IBM-3081 (i.e. 5 ms/positron).

3.2 The Positron Mode

We have used a form for the theoretical beta
spectrum given by Konopinski and Rose[27].
The energy spectra of the radioisotopes were
generated using the Fermi functions tabulation
of Fano[28], corrected for the screening
effect. The spectra were introduced into EGS
in the form of look-up Tables.

Once the positron has been generated both in
position and in direction and its energy has
been sampled according to the above scheme, it
is followed within the phantom until it reaches
a lower kinetic energy cut-off (10 keV in our
case), when it is forced to annihilate at rest.
In addition to Bhabha scattering, multiple
scattering and continuous energy loss, EGS also
considers annihilation in flight as a discrete
Monte Carlo process. Depending on the source,
between 1 and 5 per cent of the positrons have
been found to annihilate in flight, consistent
with theory [29]. Because of the thermal
motion of the orbital electrons two photon
annihilation at rest is not perfectly collinear
in the laboratory. This non-collinearity is
accounted for in the present Monte Carlo study
by using a fit to the data by Colombino et
al[30], who measured an angular distribution
of 8.5×10^{-3} rad (FWHM) in water at 22°C.
The in flight angle of the annihilation quanta,
on the other hand, is accounted for in EGS by
means of kinematics. The position, energy and
direction information for the annihilation
quanta are used as input to the subsequent
two-gamma simulation phase. Other particles
(e.g., bremsstrahlung, and delta rays) are
discarded in the phantom immediately upon
production.

3.3 The Two-Gamma Mode

During the transport of the annihilation
quanta within the phantom, all charged particles
that are generated are immediately discarded.
If the photon emerges from the phantom with an
energy greater than the cut-off energy (100 keV),
it is further transported through the hexagon
detector geometry. Following an interaction in
the lead converter, the Compton- or
photo-electron is assumed to be detected by the
MWPC provided its kinetic energy is greater than

Table 2

Count Rates for the Proposed Tomograph for a Point-like Source of 400 μCi (T/A = 1)

	In Air	10 cm radius water phantom(*)
Single rate per module (c/s)	375×10^3	250×10^3
True coincidence rate per module pair (c/s)	56×10^3	18.5×10^3
True coincidence rate for the system (c/s)	168×10^3	56×10^3
Total coincidence rate for the system: T+A (c/s)	336×10^3	112×10^3

(*) As calculated by the Monte Carlo described in section 3.

200 keV. This value has been arbitrarily chosen, according to the range energy tables[31], for the wall thickness of the glass tube. If more than one such electron is produced then the one closest to the wire plane is selected.

Each event can be displayed on a graphic device and the history of the two photons can be visualized. An example is presented in Figure 2, showing two orthogonal views of the tomograph. The photons are shown as solid and dotted lines. The scattering information related to each of the two photons are printed in the two corresponding boxes, where the various interactions are indicated. For each interaction (#) various quantities are provided (S, D, T, GE1, EKE, GE2, and TD). S is the sector where the interaction took place (1-6); it assumes the value of 0 if the interaction took place in the phantom itself. D indicates the converter (first or second); T identifies the type of interaction (C for Compton, P for photoelectric). GE1 and GE2 are the photon energies before and after the interaction; EKE

is the kinetic energy of the electron. TD is the distance of the interaction point from the end of the tube. In the example presented in Figure 2, the first photon (solid line and solid box) interacts twice in sector 3: the first one produces a Compton electron of 307 keV and the second a photoelectron of 116 keV. This photon is assumed to be detected at the point where the first interaction occurred, because it is the only one over the preestablished detection threshold. The second photon (dotted line and dotted box) also makes two interactions: the first one produces a Compton electron of 209 keV in the first converter of sector 6; the second produces a photoelectron of 215 keV in the second detector of the same sector. In this case the two electrons are both above the threshold of 200 keV, but only the nearest interaction point to the wire plane (the second one) is retained as detection position.

Subsequently the intrinsic spatial resolution of the MWPC module is introduced into the overall simulation. The real detector is

#	S	D	T	GE1	EKE	GE2	TD(CM)
1	3	1	C	511	307	204	0.038
2	3	1	P	204	116		0.105

#	S	D	T	GE1	EKE	GE2	TD(CM)
1	6	1	C	511	209	302	1.146
2	6	2	P	302	215		0.089
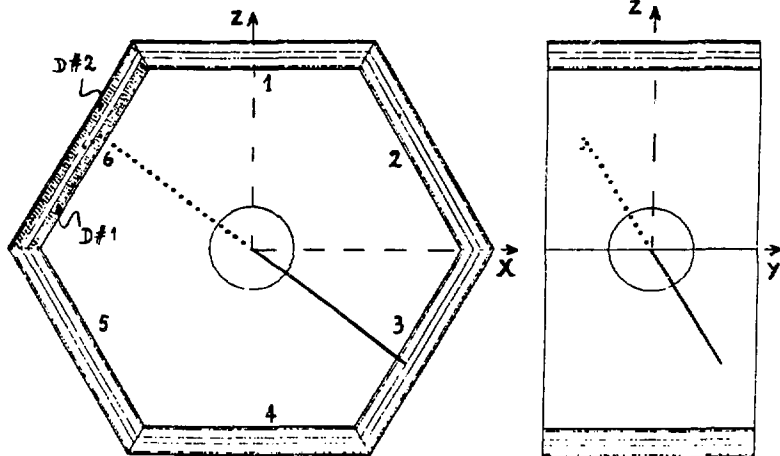
XBL 828-11166

Figure 2 - Typical Graphic display of a simulated event.

able to distinguish in which converter the interaction took place[32], but it is not able to tell where along the glass tube it occurred, generating a parallax error. This is accounted for in our simulation, by translating the actual detection point to the middle of the converter. Then the two coordinates on the wire plane are sampled according to gaussian distributions, whose FWHM has been experimentally determined (see table 1). Finally, the spatial cuts, which take into account the missing angle between two adjacent modules, are applied. (Only the events inside the active area of the detector are kept.)

3.4 Spatial Resolution Histograms

To study the spatial resolution of the Positron Camera a point-like positron source was simulated on the x-z plane (see Figure 2) at the origin. A coincidence event is defined when both photons are detected in opposite modules. For each coincidence event the line which connects the two detection points is computed. The intersection of this line with the x-z plane is calculated and its distance from the source position is accumulated in a two-dimensional histogram. Finally, a profile along any direction on the plane across the origin gives the spatial resolution distribution of the Positron Camera.

4. Monte Carlo Results

4.1 Contributions to the Spatial Resolution

Several factors contribute to the spatial resolution of the system: positron range, two-gamma non-collinearity, Compton scattering in the phantom and intrinsic detector resolution. With our Monte Carlo simulation it has been possible to study the absolute contribution of each to the overall spatial resolution; the results, which have obtained for a 10 cm radius water phantom, are now discussed in turn.

Positron Range – The radioisotopes studied are listed in Table 3 together with their main parameters and the maximum path length[33]. The range distributions are non-gaussian in shape and have a very long tail, especially for the high energy positron emitters. The effect of the positron range is best described by giving both the FWHM and the FW(0.1)M of the spatial distributions obtained in the simulation. Also included in Table 3 are the radii of the spheres which contain 50% (r_{50}) and 95% (r_{95}) of the annihilation points. These numbers have been found to be in

good agreement with experimental measurements[34]. In general r_{95} is found to be ~1/2 of the maximum path length.

Two-gamma non-collinearity – To a first approximation, an angular spread at the detector plane ($\Delta\delta$) will cause a spatial deviation at the image plane of $-R_{\Delta\delta}/2$, where R is the distance between the two planes. From the Monte Carlo results we have found a FWHM of 2.2 mm and a FW(0.1)M of 7.1 mm. The contribution from annihilation in flight, which is isotope dependent, is negligible (< 1% for ^{11}C).

Compton scattering in the phantom – Contrary to a crystal-type detector, the efficiency of a dense drift space MWPC diminishes with decreasing energy of the incident photon[35,36]. For this reason, Compton scattering is much less important here than for scintillation cameras. For a 10 cm radius water phantom both single and coincidence rates are reduced by a factor 1.5 and 3, respectively (see Table 2). Furthermore, approximately one third of the coincidence events are uniformly distributed within the phantom, whereas the smearing of the spatial resolution is negligible (< 0.1 mm FWHM).

Detector response – To a first approximation parallax error has a triangular distribtuion at the detector plane with a FWHM of $t\sqrt{A}/R$, where t is the converter thickness, A is the area of the module and R is the distance from the source. The positional deviation at the image plane will then be -1.5 mm (t = 2 cm, A = 45 × 45 cm², R = 50 $\sqrt{3}/2$ cm). From the Monte Carlo simulation we obtain a FWHM of 2.4 mm and a FW(0.1)M of 4.8 mm. The intrinsic spatial resolution of the MWPC for both x- and y-coordinates ($\Delta x = \Delta y$ - 2.0 mm FWHM, see Table 1) introduces an additional contribution of $-1/\sqrt{2}$ $(\Delta x^2 + \Delta y^2)^{1/2}$ ≈ 2.0 mm FWHM.

Overall spatial resolution of the system – The various contributions and the overall spatial resolution of the system are given in Table 4 for a ^{11}C point-like source at a center of a 10 cm radius water phantom. The overall spatial resolution values, which are obtained by adding the FWHM values in quadrature, are smaller than the calculated Monte Carlo values, as expected for the following reasoning: one cannot simply add non-gaussian distributions in quadrature. The Monte Carlo simulation, however, performs the convolution integration correctly. Similarly, for the other radioisotopes, the overall spatial resolution ranges from 4.8 mm (FWHM) for ^{18}F to 8.2 mm (FWHM) for ^{82}Rb.

Table 3

Positron Emitters Characteristics, Range and Contribution to the Spatial Resolution

	18_F	11_C	15_O	38_K	82_{Rb}
Mean life (m)	109.8	20.38	2.03	7.61	1.25
End-point of the β spectrum (MeV)	0.635	0.961	1.723	2.630	3.335
Maximum path length in water[33] (mm):	2.40	4.09	8.14	12.93	16.57
Range contribution to the spatial resolution:					
FWHM (mm)	0.3	0.4	0.7	1.2	2.0
FW(0.1)M (mm)	1.2	1.6	3.3	6.0	8.5
r_{50} in water (mm)	0.31	0.60	1.47	2.76	3.91
r_{95} in water (mm)	0.98	1.72	3.75	6.50	8.86

Table 4
Contribution to the Positron Camera Spatial
Resolution

	FWHM(mm)
Positron range	0.4
Two gamma non-collinearity	2.2
Detector response:	
– Parallax error	2.4
– Intrinsic spatial resolution	2.4
Overall spatial resolution	5.5

5. Radioisotope Distribution Reconstruction: Limited Angle Data

The radioisotope distribution within the object that we determine from the coincidence pair distributions measured in the camera is obtained by a Fourier Inversion technique[37]. Additionally, in order to achieve the best reconstruction with data subject to statistical fluctuations, we use a smoothing algorithm due to Phillips[38].

The Fourier Inversion method as such would be satisfactory if the camera were truly a six-sided box with no gaps in detection efficiency at the junctions of the detector sides. From a practical point of view, for simplicity in construction we allow an estimated gap of ~5° at the vertices of the hexagonal detector slots (Figure 1) — amounting to a total missing angle of ~30°.

It can be shown that the solid angle in front and back perpendicular to the axis of the hexagon contributes only to a loss of detection efficiency, since annihilation γ-rays going in those directions are not recorded. It does not contribute to any artifacts in the reconstruction so long as the object is smaller than the length of the sensitive area of the hexagon. On the other hand, if no provision is made for adequate treatment of the 30° azimuthal angle missing information, the quality of the reconstruction suffers and line artifacts will be created.

We summarize below the limited angle Fourier Inversion algorithm that we have developed and will use in this camera.

Let $\phi_o(r)$ be the point response of the detector system. In what follows we ensure that

$\phi_o(r)$ is space invariant — i.e. that every point within the object has the same detection efficiency — by restricting the cone of directions which we accept for the reconstruction.

Then we can write the following convolution
$$\phi(r) = \int \phi(r')\phi_o(r - r') \, d^3r' \qquad (7)$$
where $\phi(r)$ is the measured distribution of counts, and $\phi(r')$ is the unknown radioisotope distribution within the object. From the Fourier Convolution theorem we can write:
$$\phi(p) = \phi(p)\phi_o(p); \; \phi(p) = \phi(p)/\phi_o(p) \quad (8)$$

$$\phi(r) = \int \phi(p) \, e^{-2\pi i p r} \, d^3p \qquad (9)$$

If we use the Phillips smoothing algorithm equation (8) becomes

$$\phi(p) = \frac{\phi(p)}{\phi_o(p) + \gamma(2\pi)^4 p^4/\phi_o(p)} \qquad (10)$$

The parameter γ is an adjustable parameter that depends on the statistical noise level. Increasing γ makes the solution smoother but eliminates fine details of the image. In practice we constrain γ to be consistent with the spatial resolution determined by the desired pixel size on the reconstruction.

Note that in equation (10) $\phi(p)$ is not defined for Fourier components in the missing angles, i.e. the directions in the Fourier space corresponding to those in which the camera has gaps. Using the Phillips algorithm, Eq. (10), leads to the result that $\phi(p) = 0$ for the missing angles in the Fourier plane. This permits the integral in (9) to be calculated unambiguously; however, the result is a poor approximation to the real distribution and creates a number of line artifacts for each point in the object[39].

The method for approximating the missing Fourier components outlined below depends on the fact that the object source distribution is in a finite volume and has a finite maximum. From mathematical principles it is well known that, for such distributions, knowledge of the Fourier components in a limited region determines their values over all space, since the Fourier distribution in this case is a complete function. The computative algorithm is based on a similar algorithm due to Gerchberg[40] and
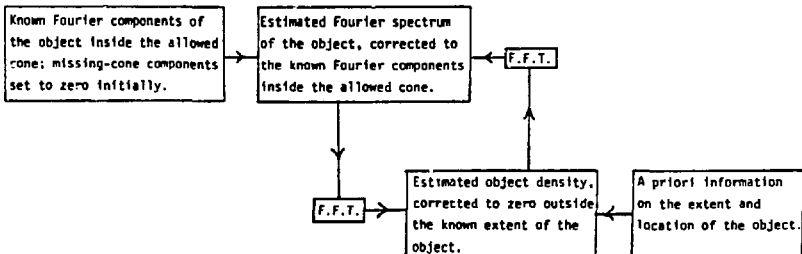

Figure 3 – The computer iteration scheme.

XBL 828-11171

applied to electrical signals by Papoulis[41].
Figure (3) shows the computer iteration scheme
used for this purpose. On a test object
simulation in our camera, for a circular phantom
of 20 cm diameter reconstructed in 6x6x10 mm³
voxels, and using a count of 400 counts/voxel we
obtained an appreciable reduction in the error
of the reconstruction compared with the test
object simulation.

6. Concluding Remarks

The tomograph we propose has an intrinsic
multislice capability: fields of view of 20-30
cm can be easily accomodated. Furthermore, the
solid angle coverage (~50%) and the possibility
of detecting off-plane photon pairs allows for
less activity, thus reducing the dose delivered
to the patient. In 3 min as many as 1×10^6
true coincidence events may be collected per
slice, if a source of 400 μCi is uniformly
distributed in a typical head phantom (Table 5),
and as many as 10 simultaneous slices may be
obtained for a total of 10×10^6 coincidence
events. Approximately the same number of events
are collected in the same time with the
three-plane NEUROCAT Tomograph[42] with a
higher activity source. The signal to noise
ratio for the MWPC solution is worse than for
NEUROCAT, but a better spatial resolution (5-6
mm FWHM) may be claimed, and systems with
resolution better than 7 mm FWHM are now
required for both brain and heart imaging[43].

Table 5
True Coincidence Rates for an Activity of
$0.1 \mu Ci/ml$ in a 10 cm Radius,
10 cm Long Water Phantom

Total True coincidence rate	56000 c/s
Number of simultaneous slices	
(1 cm thick)	10
True coincidence rate per slice	5600 c/s
Spatial resolution (FWHM)	5.5 mm
Number of voxels per slice	
$(0.6 \times 0.6 \times 1$ cm³$)$	~870
True coincidence rate per voxel	400 c/m
Compton distributed noise	~1/3

References

(1) G.N. Hounsfield, "Computerized Transverse
axial scanning (Tomography): Part I.
Description of System", Brit. J. Radiol., Vol.
46, pp. 1016-1022, 1973.
(2) A.M. Cormack, "Reconstruction of Densities
from their Projections, with Applications in
Radiological Physics", Phys. Med. Biol., Vol 18,
pp. 195-207, 1973.
(3) D.E. Kuhl and R.Q. Edwards, "Image
separation radioisotope scanning," Radiology,
Vol. 80, pp. 653-661, 1963.
(4) D.E. Kuhl and R.Q. Edwards, "The Mark IV
system for quantitative reconstruction of brain
radioactivity," J. Nucl. Med., Vol. 16,
Abstract, p. 543, 1975.
(5) C.A. Burnham and G.L. Brownell, "A
multicrystal positron camera," IEEE Trans. Nucl.
Sci., Vol. NS-19, No. 3, 201-205, 1972.

(6) M.M. Ter-Pogossian, M. Phelps, and E.J.
Hoffman, "A positron emission transaxial
tomograph for nuclear imaging (PETT),"
Radiology, Vol. 114, pp. 89-98, 1975.
(7) C.J. Tompson, Y.L. Yamamoto, and E. Meyer,
"A positron imaging system for the measurement
of regional cerebral blood flow," in Proc. Soc.
Photo-Opt. Instrum. Eng., Vol. 96, pp. 263-268,
1976.
(8) Z.H. Cho, J.K. Chan, and L. Eriksson,
"Circular ring transverse axial positron camera
for 3-dimensional reconstruction of
radio-nuclide distributions," IEEE Trans. Nucl.
Sci., Vol. NS-23, pp. 613-622, 1976.
(9) S.E. Derenzo, T.F. Budinger, J.L. Cahoon,
R.H. Huesman, and H.G. Jackson, "High resolution
computed tomography of positron emitters," IEEE
Trans. Nucl. Sci., Vol. NS-24, pp. 544-558, 1977.
(10) C. Bohm, L. Eriksson, M. Bergstrom, J.
Litton, R. Sundman, and M. Singh, "A Computer
assisted ring detector positron camera system
for reconstruction tomography of the brain,"
IEEE Trans. Nucl. Sci., Vol. NS-25, pp. 624-637,
1978.
(11) N.A. Mullani, M.M. Ter-Pogossian, C.S.
Higgins, J.T. Hood, and D.C. Ficke,
"Engineering aspects of PETT V", IEEE Trans.
Nucl. Sci., Vol. NS-26, pp. 2703-2706, 1979.
(12) L. Eriksson, Chr. Bohm, M. Bergstrom, K.
Ericson, T. Greitz, J. Litton, and L. Widen,
"One year experience with a high resolution ring
- detector positron camera system: present
status and future plans", IEEE Trans. Nucl.
Sci., Vol. NS-27, pp. 435-444, 1980.
(13) S.E. Derenzo, T.F. Budinger, R.H. Huesman,
J.L. Cahoon and T. Vuletich, "Imaging properties
of a Positron Tomograph with 280 BGO crystals",
IEEE Tans. Nucl. Sci., Vol. NS-28, pp. 81-89,
1981.
(14) E. Hoffman, M. Phelps, S. Huang, D.
Plummer and D. Kuhl, "Evaluating the Performance
of Multiplane Positron Tomographs designed for
Brain Imaging", IEEE Trans. Nucl. Sci., Vol.
NS-29, pp. 469-473, 1982.
(15) R. Allemand, C. Gresset, and J. Vacher,
"Potential advantages of Cesium Fluoride
Scintillator for a time-of-flight positron
camera", J. Nucl. Med., Vol. 21, pp. 153-155,
1980.
(16) D. Ficke, D. Beecher, G. Hoffman, J. Hood,
J. Markham, N. Mullani, and M. Ter-Pogossian,
"Engineering Aspects of PETT VI", IEEE Trans.
Nucl. Sci., Vol. NS-29, pp. 474-478, 1982.
(17) M. Yamamoto, D.C. Picke, M. Ter-Pogossian,
"Performance study of PETT VI, a Positron
computed Tomograph with 288 Cesium Fluoride
Detectors", IEEE Trans, Nucl. Sci., Vol. NS-29,
pp. 529-533, 1982.
(18) G.K. Lum, M.I. Green, V. Perez-Mendez and
K.C. Tam, "Lead Oxide Glass Tubing Converters
for Gamma Detection in MWPC", IEEE Trans. Nucl.
Sci., Vol. NS-27, pp. 157-165, 1980.
(19) P. Lecomte, V. Perez-Mendez and G. Stoker,
Electromagnetic Delay Lines in Spark,
Proportional and Drift Chamber Applications",
Nucl. Instr. and Meth., Vol. 153, pp. 543-551,
1978.
(20) G.K. Lum, V. Perez-Mendez, and B.
Sleaford, "Gamma-Ray Detection with PbO Glass

Converters in MWPC: Electron Conversion
Effficiency and Time Resolution", IEEE Trans.
Nucl. Sci., Vol. NS-28, pp. 821-824, 1981.
(21) A. Del Guerra, C.B. Lim, G.K. Lum, D.
Ortendahl, and V. Perez-Mendez, "Medical
positron imaging with a dense drift space Multi-
Wire Proportional Chamber", Lawrence Berkeley
Laboratory, LBL-14043 (March 1982), and IEEE
Trans. Med. Imag., Vol. TMI-1, 1982, in press.
(22) A. Del Guerra, V. Perez-Mendez, G.
Schwartz, and B. Sleaford, Lawrence Berkeley
Laboratory, LBL-14044 (March 1982), and
Proceedings of the "Int. Conf. on Applications
of Physics to Medicine and Biology", Trieste
(Italy), 30 March - 3 April 1982, Ed. by: G.
Alberi, Z. Bajzer, and P. Baxa, World Scientific
Publishing Co., Singapore, 1982, in press.
(23) T.A. Mulera, and V. Perez-Mendez,
"Observation of Large Saturated Pulses in Wire
Chambers with Argon-Carbon Dioxide Mixtures",
Lawrence Berkeley Laboratory, LBL-14043, (1982),
and to be published in Nucl. Instr. and Method,
1982.
(24) T.A. Mulera, A. Del Guerra, V.
Perez-Mendez, and G. Schwartz, "Large Signal
Production in Wire Chambers Filled with Noble
Gas-Carbon Dioxide and Noble-Gas Hydrocarbon
Mixtures", Lawrence Berkeley Laboratory,
LBL-14412 (1982), and to be presented at the
1982 IEEE NS-Symposium, Washington, D.C.,
October 20-22, 1982.
(25) R. L. Ford and W. R. Nelson, "The EGS Code
system: Computer program for the Monte Carlo
Simulation of Electromagnetic Cascade Showers
(Version 3)", Stanford L. ar Accelerator
Center, SLAC-210, June 19.8.
(26) W.R. Nelson, and T.M. Jenkins, editors,
"Computer Techniques in Radiation Transport and
Dosimetry", Plenum Press, New York, 1980.
(27) E. J. Konopinski, and M.E. Rose, "The
Theory of Nuclear β-decay", in Alpha-, Beta-,
Gamma-Ray Spectroscopy", ed. K. Siegbahn,
North-Holland Publ. Co., Amsterdam, 1965, pp.
1327-1364.
(28) U. Fano "Tables for the Analysis of Beta
Spectra", National Bureau of Standards, Applied
Mathematics Series, Vol. 13, 1952.
(29) W. Heitler, "The Quantum Theory of
Radiation", Clarendon Press, Oxford, 1954,
pp. 270-271.
(30) P. Colombino, B. Fiscella, and L. Trossi,
"Study of Positronium in Water and Ice from 22
to -144°C by Annihilation Quanta Measurements",
Nuovo Cimento, Vol. 38, pp. 707-723, 1965.
(31) L. Katz, and A.S. Penfold, "Range-theory
Relations for Electrons and the Determination of
Beta-Ray End-Point Energies by Absorption", Rev.
Mod. Phys., Vol 24, pp. 28-44, 1952.
(32) A. Del Guerra, V. Perez-Mendez, G.
Schwartz, and W.R. Nelson, "Design
Considerations for a High Spatial Resolution
Positron Camera", Lawrence Berkeley Laboratory
Report, LBL-14414 (1982), and to be presented at
the 1982 IEEE NS-Symposium, Washington D.C.,
October 20-22, 1982.
(33) H.J. Berger and S.M. Seltzer, "Table of
Energy Losses and Ranges of Electrons and
Positrons", National Aeronautics and Space
Administration Report, NASA - SP - 3012, 1964.

(34) S.E. Derenzo, "Precision Measurement of
Annihilation Point Spread Distributions for
Medically Important Positron Emitters", in
Proceedings on the "5th International Conference
or Positron Annihilation", Sendai, Japan, The
Japan Institute of Metals, pp. 819-823, 1979.
(35) A.P. Jeavons, G. Charpak, and R.J. Stubbs,
"The High-Density MultiWire Drift Chamber",
Nucl. Instr. and Meth., Vol. 124, pp. 491-503,
1975.
(36) D. Chu, K.C. Tam, V. Perez-Mendez, C.B.
Lim, D. Lambert, and S.N. Kaplan,
"High-Efficiency Collimator - Converters for
Neutral Particle Imaging with MWPC", IEEE Trans.
Nucl. Sci., Vol. NS-23, pp. 634-639, February
1976.
(37) K.C. Tam and V. Perez-Mendez,
"Tomographical Imaging with Limited-Angle
Input", J.Opt. Soc. Am., Vol. 71, pp. 582-592,
1981.
(38) D.L. Phillips, "A Technique for Numerical
Solution of Certain Integral Equations", J.
Assoc. Comp. Mach. Vol. 9, pp. 84-97, 1962.
(39) K.C. Tam and V. Perez-Mendez, "Limited
Angle Three Dimensional Reconstructions Using
Fourier Transform Iterations and Radon Transform
Iterations", Opt. Eng., Vol. 20, pp. 586-589,
1981.
(40) R.W. Gerchberg, "Super Resolutions Through
Energy Error Reduction", Opt. Acta, Vol. 21, pp.
709-720, 1974.
(41) A. Papoulis, "The Fourier Integral and Its
Applications", McGraw-Hill, New York, 1962,
p. 44.
(42) E.J. Hoffman, M.E. Phelps, and S.C. Huang,
"Performance Evaluation of a Positron Tomograph
Designed for Brain Imaging", Department of
Radiological Sciences, UCLA, School of Medicine,
Report, 1982.
(43) T.F. Budinger, S.E. Derenzo, R.H. Huesman,
and J.L. Cahoon, "Positron Emission Tomography:
Instrumentation Perspectives", in Proceedings of
the "Int. Workshop on Physics and Engineering in
Medical Physics", March 15-18, 1982, Pacific
Grove, California, IEEE Computer Society Press,
pp. 3-13, 1982.